J. Fluid Mech. (2002), *vol.* 458, *pp.* 153–180. © 2002 Cambridge University Press
DOI: 10.1017/S0022112002007917 Printed in the United Kingdom

Linear stability of rectangular cavity flows driven by anti-parallel motion of two facing walls

By S. ALBENSOEDER AND H. C. KUHLMANN

ZARM, Universität Bremen, 28359 Bremen, Germany

(Received 18 October 2001)

The flow in an infinite slab of rectangular cross-section is investigated numerically by a finite volume method. Two facing walls which move parallel to each other with the same velocity, but in opposite directions, drive a plane flow in the cross-section of the slab. A linear stability analysis shows that the two-dimensional flow becomes unstable to different modes, depending on the cross-sectional aspect ratio, when the Reynolds number is increased. The critical mode is found to be stationary for all aspect ratios. When the separation of the moving walls is larger than approximately twice the height of the cavity, the basic flow forms two vortices, each close to one of the moving walls. The instability of this flow is of centrifugal type and similar to that in the classical lid-driven cavity problem with a single moving wall. When the moving walls are sufficiently close to each other (aspect ratio less than 2) the two vortices merge and form an elliptically strained vortex. Owing to the dipolar strain this flow becomes unstable through the elliptic instability. When both moving walls are very close, the finite-length plane-Couette flow becomes unstable by a similar elliptic mechanism near both turning zones. The critical mode produces wide streaks reaching far into the cavity. For a small range of aspect ratios near unity the flow consists of a single vortex. Here, the strain field is dominated by a four-fold symmetry. As a result the instability process is analogous to the instability of a Rankine vortex in an quadripolar strain field, resulting from vortex stretching into the four corners of the cavity.

1. Introduction

The flow of an incompressible Newtonian fluid in simple bounded domains is of fundamental interest, because the dynamical problem is free from unnecessary geometrical complications. Yet, essential wall effects are included. Such systems can thus provide insight into the basic mechanisms that are operative in more specific flow problems arising in technical applications.

Here we consider a class of vortex flows in rectangular containers of infinite span. The motion is driven by two facing sidewalls of the container which slide with constant and equal speed, but in opposite directions. By variation of the cross-sectional aspect ratio this system can model a variety of situations ranging from the interaction of two co-rotating wall-bounded vortices to finite-length plane-Couette flow. The system is an extension of the classical lid-driven cavity problem (see e.g. Shankar & Deshpande 2000 and Albensoeder, Kuhlmann & Rath 2001*a*, *b*) and may serve as a model for certain coating flows (Benjamin, Anderson & Scriven 1995).

The Stokes flow in a rectangular two-sided lid-driven cavity with free-surface

https://doi.org/10.1017/S0022112002007917 Published online by Cambridge University Press

sidewalls has been investigated by Gaskell *et al.* (1996, 1998) who used a finite-element and a biharmonic series-expansion method, respectively. Their concern was the topology of the creeping flow. The same problem, but with rigid sidewalls has been considered by Kelmanson & Lonsdale (1996) using an integral-equation method. Likewise, these authors were interested in the eddy genesis in creeping flow. These investigations did not include the effects of inertia, even though inertia plays a crucial role in the existence of multiple solutions in the two-sided lid-driven cavity. Such multiple two-dimensional steady flow states were found by Kuhlmann, Wanschura & Rath (1997) and they have been explored more systematically by Albensoeder *et al.* (2000*a*). The latter authors discovered up to seven different flow states in the cavity depending on the aspect ratio and the two side-wall Reynolds numbers.

To date, all three-dimensional stability analyses of lid-driven cavity flows have focused mainly on the classical one-sided lid-driven cavity in which a single lid drives the flow. Numerical attempts to calculate the linear stability boundaries of the steady two-dimensional basic flow are due to Ramanan & Homsy (1994) and Ding & Kawahara (1998, 1999). But the problem was not solved until the work of Albensoeder *et al.* (2001*b*), who provided accurate linear-stability boundaries, i.e. critical Reynolds numbers, for a wide range of aspect ratios and who showed that four different instabilities may occur which are all due to centrifugal effects.

One of the first investigations of the nonlinear flow in cavities with two moving walls is due to Kuhlmann *et al.* (1997) who carried out experiments in a cavity in which the separation of the moving walls was about twice the distance between the stationary walls (aspect ratio $\Gamma = 1.96$). They found a supercritical instability to a three-dimensional flow consisting of rectangular steady cells. By a linear stability analysis for a limited range of aspect ratios it was shown that the instability for anti-parallel wall motion is due to the strain in the centre of the vortex. These results have been extended by Blohm & Kuhlmann (2002) who carefully measured the steady and time-dependent bifurcations which occur at higher Reynolds numbers. The case of parallel wall motion has been investigated numerically by Albensoeder & Kuhlmann (2002). For a two-sided lid-driven cavity with differentially heated moving walls Alleborn, Raszillier & Durst (1999) calculated the basic flow, including the heat and mass transfer, and its linear stability with respect to the limited class of two-dimensional perturbations. Moreover, the system's relevance to industrial drying processes was pointed out.

The instability in the two-sided lid-driven cavity found by Kuhlmann *et al.* (1997) resembles the instability of elliptic vortices in unbounded flows. The authors pointed out the similarity of the nonlinear steady cellular flow observed in the cavity with the structure of the early transient flow of an elliptic vortex (flattened Taylor–Green vortex) decaying to turbulence which has been calculated numerically by Lundgren & Mansour (1996). In particular, the vorticity was found to be distorted into sheet-like structures in both cases. Sipp & Jacquin (1998) employed both short-wave asymptotics and classical linear stability theory to calculate the instability of flattened Taylor–Green vortices. They found that the streamlines in the centre of the elliptical vortex are the most unstable ones, which is consistent with the peak of the energy transfer to the perturbation in the unstable cavity flow considered by Kuhlmann *et al.* (1997), and that the structure of the most unstable perturbation is identical to that of the critical mode in homogeneous elliptic flow (Waleffe 1990). Moreover, the nonlinear temporal development calculated by Sipp & Jacquin (1998) is analogous to the simulation result of Lundgren & Mansour (1996).

In the limit of a small distance between the two moving walls the two-dimensional

https://doi.org/10.1017/S0022112002007917 Published online by Cambridge University Press

flow in the central region of the cavity approaches plane-Couette flow. The transition to turbulence in this classical problem is still under investigation today; see e.g. Manneville & Dauchot (2001). In experimental realizations, finite-length systems must be employed and the inevitable end conditions are usually not very well defined. Typically, the gap widens into a larger volume of fluid as in the apparatus used by Taylor (1934) for the stretching of droplets suspended in a carrier fluid. Modern experiments (Tillmark & Alfredsson 1992) use a similar setup with open ends. In such experiments, the measurement time is severely limited by the propagation of disturbances from the open ends into the bulk, eventually leading to a premature transition to turbulence. End effects in finite-length systems must therefore always be taken into account.

The present paper is a systematic extension of the work of Kuhlmann *et al.* (1997). We shall investigate the linear stability of the basic two-dimensional flow in two-sided lid-driven cavities, paying particular attention to the influence of the cross-sectional aspect ratio. The methods of investigation are introduced in § 2, in which the problem is defined, the numerical procedures described, and the numerical code is validated. An overview on the critical conditions in § 3 is followed by a detailed explanation of each type of instability that can arise. The energy-transfer mechanisms are elucidated and the structures of the different neutral modes are discussed. A conclusion in § 4 summarizes our results.

2. Methods of investigation

2.1. *Problem formulation*

We consider the incompressible flow of a Newtonian fluid in a rectangular volume of height h and width d in the (x, y)-plane. The geometry is sketched in figure 1. The domain is assumed to be infinitely extended in the third (z) direction. The fluid motion is driven by two opposing sidewalls at $x = \pm d/2$ which move with the same constant speed V, but in opposite directions. Length, velocity, time, and pressure are scaled using h, v/h, h^2/v, and $\rho v^2/h^2$, where v is the kinematic viscosity and ρ the density of the fluid. In this scaling, the Navier–Stokes and continuity equations are given by

$$\frac{\partial \boldsymbol{u}}{\partial t} + \boldsymbol{u} \cdot \nabla \boldsymbol{u} = -\nabla p + \nabla^2 \boldsymbol{u}, \tag{2.1}$$

$$\nabla \cdot \boldsymbol{u} = 0. \tag{2.2}$$

The no-slip, no-penetration boundary conditions for $\boldsymbol{u}$ read

$$\boldsymbol{u}(y = \pm 1/2) = 0 \quad \text{and} \quad \boldsymbol{u}(x = \pm \Gamma/2) = \mp Re\, \boldsymbol{e}_y, \tag{2.3}$$

where the two governing parameters are the Reynolds number Re and the aspect ratio Γ:

$$Re = \frac{Vh}{v} \quad \text{and} \quad \Gamma = \frac{d}{h}. \tag{2.4}$$

Note that the y-direction is always defined parallel to the moving walls (also in the limit $\Gamma \to 0$).

2.2. *Basic flows*

For small Reynolds numbers the flow will reflect the translational invariances in z and t of the governing equations and be two-dimensional and steady. As the Reynolds

https://doi.org/10.1017/S0022112002007917 Published online by Cambridge University Press

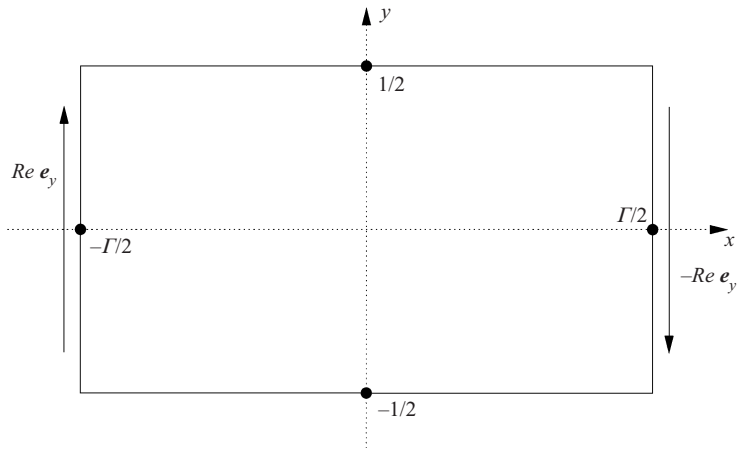


FIGURE 1. Cross-section of the slab in the (x, y)-plane.

number increases and inertia terms become increasingly important, multiple two-dimensional solutions may appear. Albensoeder *et al.* (2001*a*) found multiple (up to seven) two-dimensional solutions, some of which break the discrete rotational symmetry by an angle of π about the z-axis. The existence of multiple two-dimensional states is an important feature, because all of these states must be considered separately when a complete stability analysis is to be performed. It will turn out, however, that this complication arises only in a small range of aspect ratios. Therefore, we shall indicate all basic steady solutions $(\boldsymbol{u}_0(x, y), p_0(x, y))$ of (2.1), (2.2) by a subscript 0. It will be mentioned explicitly when this state is not unique.

2.3. *Stability analysis*

The linear stability of any of the two-dimensional steady basic flows is governed by

$$\frac{\partial \boldsymbol{u}}{\partial t} + \boldsymbol{u}_0 \cdot \nabla \boldsymbol{u} + \boldsymbol{u} \cdot \nabla \boldsymbol{u}_0 = -\nabla p + \nabla^2 \boldsymbol{u}, \tag{2.5}$$

$$\nabla \cdot \boldsymbol{u} = 0, \tag{2.6}$$

where $\boldsymbol{u}$ and p denote the deviation from the particular basic state $(\boldsymbol{u}_0, p_0)$ under consideration. The perturbation flow is subject to no-slip and no-penetration boundary conditions on all walls, $\boldsymbol{u}(x = \pm 1/2) = \boldsymbol{u}(y = \pm \Gamma/2) = 0$. Owing to the infinite extension in the z-direction the perturbation modes can be written as normal modes

$$\begin{pmatrix} \boldsymbol{u} \\ p \end{pmatrix}(x, y, z, t) = \begin{pmatrix} \boldsymbol{U} \\ P \end{pmatrix}(x, y) \exp\{\sigma t + \mathrm{i}(\omega t - kz)\} + \text{c.c.}, \tag{2.7}$$

where $\sigma, \omega, k \in \mathbb{R}$. The critical Reynolds number Re_c is determined by the condition that the maximum possible growth rate vanishes. Hence the growth rate σ must be maximized over all discrete modes (numbered by q) and all continuous wavenumbers k, i.e. $\max_{k,q} \sigma(k, q, Re_c, \Gamma) = 0$. Modes for which only $\sigma(Re_n, \Gamma) = 0$, are called neutral modes with the neutral Reynolds number Re_n. The growth rates σ are determined by a large generalized eigenvalue problem which results from (2.5), (2.6) after an appropriate discretization. The eigenvectors represent the corresponding discretized flow and pressure fields $(\boldsymbol{U}, P)$.

https://doi.org/10.1017/S0022112002007917 Published online by Cambridge University Press

2.4. *Energy analysis*

For a discussion of the instability mechanisms, an *a posteriori* evaluation of the energy budget of the critical modes has proven very useful (Kuhlmann *et al.* 1997; Albensoeder *et al.* 2001*b*). The rate of change of the kinetic energy E_{kin} can be written as

$$\frac{1}{D_*}\frac{\mathrm{d}E_{\mathrm{kin}}}{\mathrm{d}t} = -1 + \sum_{i=1}^{4}\int_V I_i \,\mathrm{d}V = -1 + \sum_{i=1}^{4}\int_V I_i' \,\mathrm{d}V, \tag{2.8}$$

where D_* is the total dissipation in the volume

$$D_* = \int_V (\nabla \times \boldsymbol{u})^2 \,\mathrm{d}V, \tag{2.9}$$

and the integrals are taken over the volume V occupied by the fluid. The energy production rates can be decomposed in different ways. Depending on the particular instability either the usual decomposition into Cartesian coordinates, describing the momentum transport in the Cartesian directions, or a decomposition into longitudinal and transversal contributions, describing the momentum transport parallel and perpendicular to the local basic-flow direction, can be used. Accordingly, we introduce the Cartesian decomposition of the local production rate $-\boldsymbol{u}\cdot(\boldsymbol{u}\cdot\nabla\boldsymbol{u}_0)$ normalized by the dissipation D_* as

$$\sum_{i=1}^{4} I_i = -\frac{1}{D_*}\left(uu\frac{\partial u_0}{\partial x} + uv\frac{\partial u_0}{\partial y} + vu\frac{\partial v_0}{\partial x} + vv\frac{\partial v_0}{\partial y}\right), \tag{2.10}$$

where i numbers all terms on the right-hand side consecutively, and the longitudinal/transversal decomposition (Albensoeder *et al.* 2001*b*)

$$\sum_{i=1}^{4} I_i' = -\frac{1}{D_*}[\boldsymbol{u}_\perp\cdot(\boldsymbol{u}_\perp\cdot\nabla\boldsymbol{u}_0) + \boldsymbol{u}_\parallel\cdot(\boldsymbol{u}_\perp\cdot\nabla\boldsymbol{u}_0) + \boldsymbol{u}_\perp\cdot(\boldsymbol{u}_\parallel\cdot\nabla\boldsymbol{u}_0) + \boldsymbol{u}_\parallel\cdot(\boldsymbol{u}_\parallel\cdot\nabla\boldsymbol{u}_0)], \tag{2.11}$$

where

$$\boldsymbol{u}_\parallel = \frac{(\boldsymbol{u}\cdot\boldsymbol{u}_0)\boldsymbol{u}_0}{{\boldsymbol{u}_0}^2} \quad \text{and} \quad \boldsymbol{u}_\perp = \boldsymbol{u} - \boldsymbol{u}_\parallel. \tag{2.12}$$

Of course, the total local production is the same in both cases, $\sum_{i=1}^{4} I_i = \sum_{i=1}^{4} I_i'$.

The well-established temporal linear-stability method yields global critical modes. Using the Reynolds–Orr equation it is possible to quantify and to localize the energy transfer and the dissipation of the critical mode. A discussion of the instability in terms of notions such as *centrifugal* or *elliptic instabilities* is made difficult for the following reasons:

(*a*) the instability characteristics may change continuously upon variation of the governing parameters such as the aspect ratio;

(*b*) no rigorous criteria exist for a classification of the instabilities of general viscous flows in terms of centrifugal instabilities, etc.; and

(*c*) the notions *centrifugal*, *elliptic* or *quadripolar instabilities* have been introduced for simple idealized flows and cannot straightforwardly be applied to instabilities of more general flows.

The short-wavelength instability analysis using the geometric-optics method introduced by Lifshitz & Hameiri (1991) may provide a more precise classification, because the instability can be traced back to the property of the basic flow in the vicinity of a single streamline. However, the short-wavelength analysis is restricted

https://doi.org/10.1017/S0022112002007917 Published online by Cambridge University Press

to asymptotically small perturbation wavelengths ($k \to \infty$). It has been shown by Bayly (1988) and Sipp, Lauga & Jacquin (1999) that it is possible to construct normal modes localized around the streamline ψ_0^*, for which the amplification rate along the streamline $\sigma(\psi_0)$ has a local maximum, in the form of an infinite series using the result of the short-wavelength analysis. To improve the convergence of this series for finite wavenumbers k, however, one must resort to higher-order asymptotics (Bayly, Orszag & Herbert 1988). If, therefore, the calculation of the critical mode with finite k is required the classical normal-mode analysis is usually preferable.

In this work we employ a normal-mode analysis and use the Reynolds–Orr equation to clarify the characteristics of the energy-transfer process. The discussion of the instability mechanism will be based on qualitative and quantitative comparisons of the features of the basic flow, the normal mode, and the energy transfer with instabilities arising in highly idealized systems such as the linear elliptic flow (Waleffe 1990).

2.5. *Numerical methods and code validation*

The numerical methods are identical to those of Albensoeder *et al.* (2001*a*, *b*). As the starting point for any stability analysis the steady basic solution $(\boldsymbol{u}_0, p_0)$ is calculated by a finite-volume-discretization method using primitive variables on a staggered grid. Surface integrals and intermediate values are calculated by the midpoint rule and linear interpolation (Ferziger & Perić 1996). In this formulation pressure boundary conditions are not required. To resolve the gradients in the near-wall regions the grid is slightly stretched near the boundaries by a stretching factor of 0.95 between neighbouring cells. While accuracy is second order for equidistant grids, it is formally lowered to first order by the grid stretching. For weak stretching, however, as in the present case, the code is nearly second-order accurate (Ferziger & Perić 1996). The resulting discretized nonlinear set of equations is solved by Newton–Raphson iteration.

To solve the linear stability problem (2.5), (2.6) the four unknowns (u, v, w, p) are discretized on the same grid as for the basic state, and the same finite-volume method is used. Inserting the discretized normal modes into the linear-stability equations leads to a large generalized eigenvalue problem which is solved by inverse iteration. All resulting linear systems of equations for the Newton–Raphson iteration and the eigenvector iteration are solved using LAPACK subroutines. All data presented were calculated on 141×141 grid points 35 of which being stretched towards each boundary.

A validation of the basic-flow calculations has been provided by Albensoeder *et al.* (2001*a*) by comparison with benchmark solutions for the classical square cavity driven by a single moving lid (Ghia, Ghia & Shin 1982; Botella & Peyret 1998). Moreover, in Albensoeder *et al.* (2001*a*) we compared the existence ranges of multiple solutions with the results of Kuhlmann *et al.* (1997) for the two-sided lid-driven cavity (see figure 2). An extensive validation of the linear stability analysis was done by Albensoeder *et al.* (2001*b*) by comparing neutral and critical stability boundaries for the classical single-lid-driven cavity with numerical (Ramanan & Homsy 1994; Ding & Kawahara 1999) and experimental (Albensoeder *et al.* 2001*b*) results. To give further weight to the present numerical code, the critical data are compared in figure 2 with those of Kuhlmann *et al.* (1997). For example, the minimum of the stability boundary shown in figure 2 occurs at $\Gamma = 1.428$, $Re_c = 189.8$, and $k_c = 2.406$. These data must be compared with those of Kuhlmann *et al.* (1997) who obtained $\Gamma = 1.45 \pm 0.05$, $Re_c = 190.4$, and $k_c = 2.4 \pm 0.05$. Albensoeder *et al.* (2001*b*) showed that the calculated

https://doi.org/10.1017/S0022112002007917 Published online by Cambridge University Press

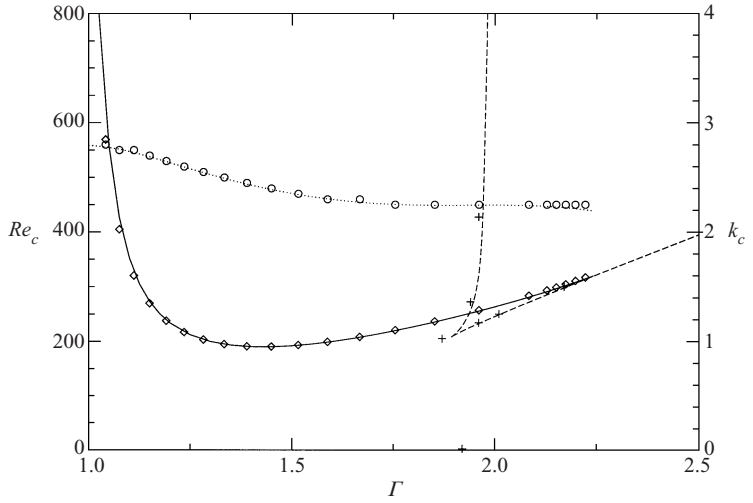


FIGURE 2. Comparison of the present results (lines) with those obtained by Kuhlmann *et al.* (1997) (symbols). Critical Reynolds number Re_c: full line and ◇; critical wavenumber k_c: dotted line and ○. The dashed line and + indicate the existence range of multiple solutions.

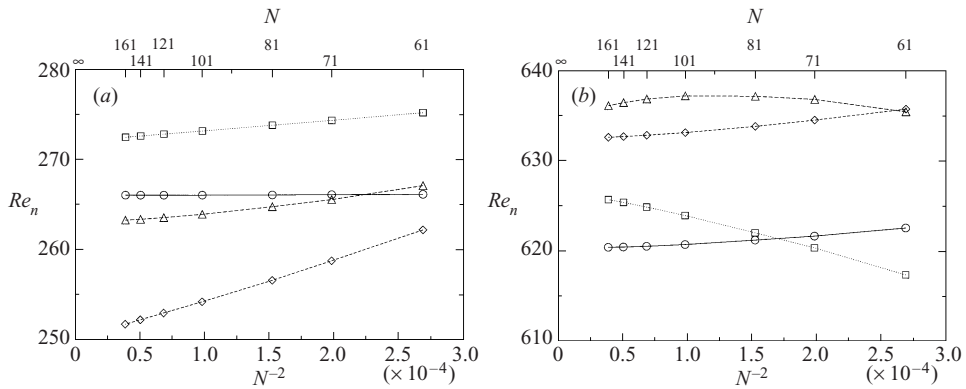


FIGURE 3. Dependence of the neutral Reynolds number Re_n on the grid resolution; here $Re_n = Re_c$. Symbols indicate different aspect ratios. (*a*) ○, $\Gamma = 0.60$ (E1); □, $\Gamma = 1.15$ (E2); ◇, $\Gamma = 2.00$ (E2); and △, $\Gamma = 2.00$ (C). (*b*) ○, $\Gamma = 0.19$ (E1); □, $\Gamma = 0.775$ (E1); ◇, $\Gamma = 0.85$ (Q); and △, $\Gamma = 1.04$ (E2). N is the square root of the total number of grid points. The notations E1, E2, Q, and C indicate different instability branches. They are introduced in § 3.

critical Reynolds numbers deviate less than 3% from the true critical values. This conservative estimate also holds for the present calculations, the error being much less in most cases. Examples of the grid dependence of the critical parameters for the present problem are given in figure 3(*a*, *b*). Similar convergence rates apply to all critical data reported in the following.

3. Results

The main results are summarized in figure 4 which shows the linear stability boundaries and the critical wavenumbers. All data presented have been obtained for 141 × 141 grid points.† The most unstable mode is always stationary, independent

† Vector and contour plots have been interpolated to smaller grid sizes.

https://doi.org/10.1017/S0022112002007917 Published online by Cambridge University Press

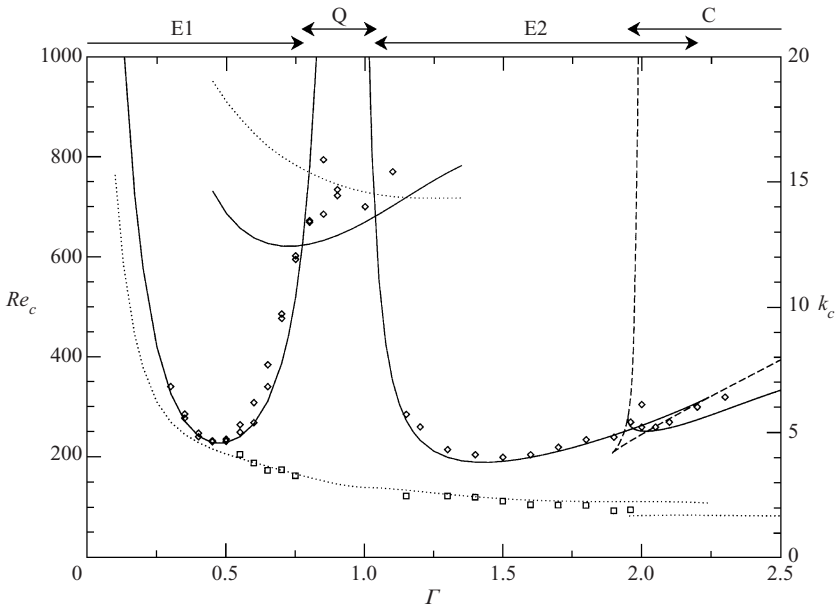


FIGURE 4. Critical Reynolds numbers Re_c (envelope of the full lines) and wavenumbers k_c (dotted lines) as functions of the aspect ratio Γ. Different segments of the critical curve between the intersection points of the neutral curves are denoted by capital letters on top of the figure. The dashed line indicates the existence range of multiple (three) two-dimensional solutions. Experimental critical data for Re_c ($\diamond$) for k_c ($\square$) have been taken from Blohm *et al.* (2001).

of the aspect ratio. The critical curve is made up of sections of different neutral curves.

For small aspect ratios the basic flow becomes unstable via an instability denoted by E1. For the present definition of Re according to (2.4) the critical Reynolds number takes a minimum value of $Re_c = 226.4 \pm 0.2$ at $\Gamma = 0.475 \pm 0.001$ with $k_c = 4.2104 \pm 0.0004$. As a measure for the numerical uncertainty we have taken the difference between the values of a variable obtained on the present fine grid (141×141) and on a grid with half the number of grid points in each direction (71×71). The neutral branch E1 increases strongly for $\Gamma \uparrow (\approx 1)$. Beyond a maximum (not shown in figure 4) the neutral Reynolds number decreases steeply near $\Gamma \approx 1$ and forms the section of the critical curve labelled E2. The character of the instabilities E1 and E2 is very similar as they develop continuously along the neutral curve connecting both segments of the critical curve.

Near $\Gamma = 1$, where the neutral curve connecting the segments E1 and E2 reaches a rather large maximum, another instability, denoted by Q, arises. The corresponding neutral curve intersects with E1 and E2 at $(\Gamma, Re) = (0.775 \pm 0.002, 623.4 \pm 3.5)$ and $(\Gamma, Re) = (1.036 \pm 0.001, 680.4 \pm 2.4)$, respectively.

For larger aspect ratios, $\Gamma \gtrsim 2$, three different steady basic flows exist within the range outlined by the dashed curves in figures 4 and 5. Two of these basic states are linearly stable with respect to two-dimensional perturbations, while a third state is unstable in two dimensions. The multiplicity of flow states is associated with a fold of the solution manifold (Kuhlmann *et al.* 1997; Albensoeder *et al.* 2001*a*). Adopting the notation of Albensoeder *et al.* (2001*a*) for the two relevant basic states, the *strongly merged vortex state*, corresponding to an elliptical vortex flow (an example is

https://doi.org/10.1017/S0022112002007917 Published online by Cambridge University Press

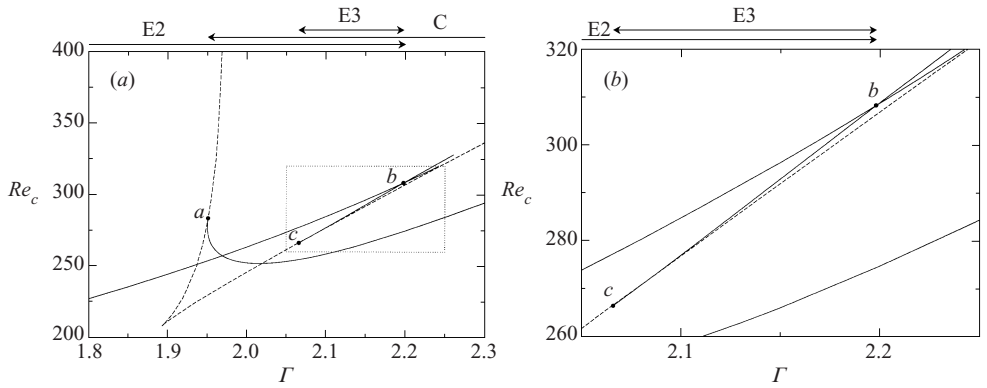


FIGURE 5. (*a*) Neutral Reynolds numbers (full lines) and existence range of triple basic-state solutions (delineated by the dashed curves) for a range of aspect ratios near $\Gamma = 2$. (*b*) Close-up of the region marked by the dotted box in (*a*).

shown in figure 9), exists to the left (smaller Γ) of the rightmost dashed line, while the *two-vortex state* which consists of two well-separated vortices exists to the right (higher Γ) of the leftmost dashed line (approximately $\Gamma \approx 2$, see Kuhlmann *et al.* 1997). Since the three-dimensional linear-stability boundaries continue into the range of two-dimensional non-uniqueness, the critical curves extend to the border of the existence range where the respective base flow ceases to exist.

For very large aspect ratios the basic state is the two-vortex flow. Its stability curve, labelled C in figure 4, terminates at $(\Gamma_a, Re_a) = (1.951 \pm 0.010, 283.5 \pm 7.0)$ on the existence boundary of the two-vortex flow (point *a* in figure 5). Conversely, the neutral stability boundary E2 terminates on the rightmost dashed line marking the largest aspect ratio for which the strongly merged vortex flow exists. Before reaching the termination point, however, the neutral curve E2 intersects with another neutral branch E3 at the point $(\Gamma_b, Re_b) = (2.198 \pm 0.003, 308.3 \pm 4.1)$ (point *b* in figure 5). The neutral curve E3 is a critical curve for the strongly merged vortex flow only in a small range of the aspect ratio. In a small wedge-shaped region (see figure 5*b*) the Reynolds numbers within which the merged flow state is linearly stable is bounded from above by E2 and from below by E3. The lower critical curve E3 finally terminates at $(\Gamma_c, Re_c) = (2.066 \pm 0.004, 266.3 \pm 3.0)$ (point *c* in figure 5) on the existence boundary of the strongly merged vortex flow.

Owing to the path of the various neutral curves, there remains only a small range of parameters within which both the strongly merged state and the two-vortex state can be observed, i.e. where both are linearly stable (cf. Kuhlmann *et al.* 1997). The instability branch C for $\Gamma > 1.951$ persists for $\Gamma \to \infty$. Some numerical values of the critical parameters are given in table 1.

Neutral curves $Re_n(k)$ for a number of aspect ratios are shown in figure 6. For small aspect ratios (full line) the bandwidth in k-space of the instability E1 is wide. As the aspect ratio increases, the critical Reynolds number increases and the bandwidth narrows considerably (long dashed line). The bandwidth of the instability Q (dash-dotted lines) is relatively wide and the neutral modes have a much larger wavenumber. Neutral curves for the instability E2 are not shown, because they have already been given by Kuhlmann *et al.* (1997). Growth rates σ of the unstable modes as a function of $(Re - Re_c)/Re_c$ are plotted in figure 7(*a*, *b*) for several aspect ratios. Figure 7(*a*) shows that the supercritical growth rates of the modes E1 and Q are typically higher

https://doi.org/10.1017/S0022112002007917 Published online by Cambridge University Press

Γ	Re_c	k_c	Type
0.30	326.3 ± 0.4	5.385 ± 0.004	E1
0.50	227.9 ± 0.3	4.114 ± 0.001	E1
1.00	669.3 ± 1.3	14.58 ± 0.040	Q
1.50	191.9 ± 1.0	2.353 ± 0.001	E2
2.00	263.3 ± 2.2	2.247 ± 0.001	E2
2.17	299.3 ± 2.8	2.024 ± 0.004	E3
2.00	252.2 ± 6.6	1.693 ± 0.011	C
2.50	334.3 ± 5.1	1.685 ± 0.012	C

TABLE 1. Critical data for selected aspect ratios. The specified uncertainty is the relative difference between the values obtained on the fine grid (141×141) and those on a grid with half the number of grid points in each direction (71×71).

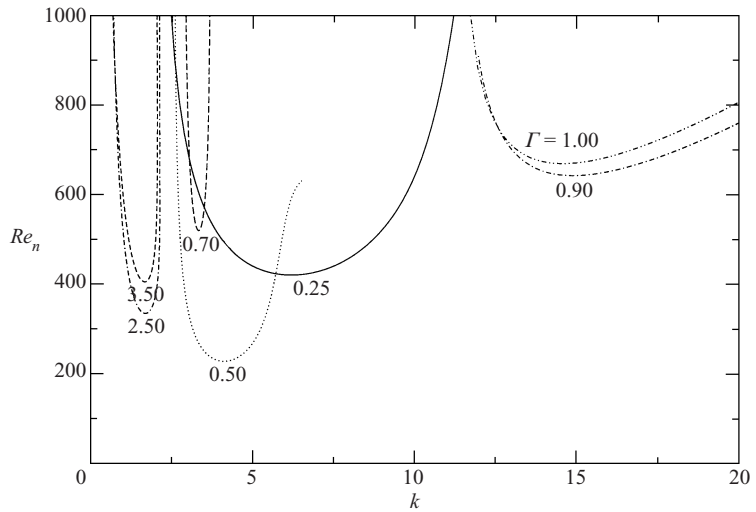


FIGURE 6. Neutral curves $Re_n(k)$ as functions of k for several aspect ratios Γ. Line styles indicate the aspect ratio. Solid: $\Gamma = 0.25$ (E1), dotted: $\Gamma = 0.50$ (E1), long-dashed: $\Gamma = 0.70$ (E1), dash-dotted: $\Gamma = 0.90$ (Q), dash-dot-dotted: $\Gamma = 1.00$ (Q), dash-dash-dotted: $\Gamma = 2.50$ (C) and short-dashed: $\Gamma = 3.50$ (C).

than those of the modes E2 and C, the growth rates of the last two modes being of the same order of magnitude. In figure 7(*b*) growth rates are given for the aspect ratios $\Gamma = 0.775$ and $\Gamma = 1.036$ corresponding to the two codimension-2 points at which the neutral curves E1 and Q, and Q and E2, respectively, intersect. Owing to the large slope of the neutral curves E1 and E2 the modes C exhibit higher supercritical growth rates than the modes E1 and E2.

3.1. *Elliptic instability for* $1.036 < \Gamma < 2.198$ (*E2*)

Along the neutral curve E2, in the aspect-ratio range $1.036 < \Gamma < 2.198$, the instability is caused by the elliptic instability mechanism. Except for aspect ratios near $\Gamma = 2$ it is the first instability.

The elliptic instability is essentially the same as the process by which a vortex filament becomes unstable when it is subject to an external plane strain (Moore & Saffmann 1975; Tsai & Widnall 1976) and by which vortex rings lose their

https://doi.org/10.1017/S0022112002007917 Published online by Cambridge University Press

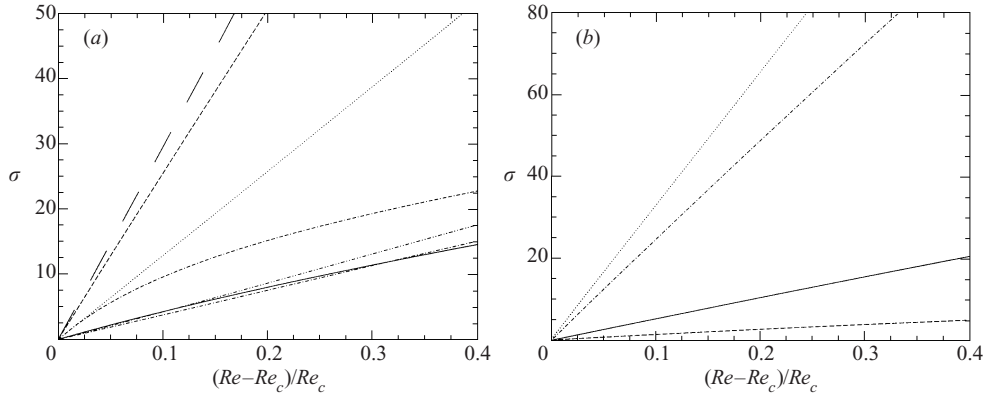


FIGURE 7. Growth rate σ as functions of $(Re-Re_c)/Re_c$ for several aspect ratios Γ. The wavenumber is kept constant at $k = k_c(\Gamma)$ (see table 1). Line styles indicate the aspect ratio. (*a*) Long-dashed: $\Gamma = 0.30$ (E1), dotted: $\Gamma = 0.50$ (E1), dashed: $\Gamma = 1.00$ (Q), solid: $\Gamma = 1.50$ (E2), dash-dash-dotted: $\Gamma = 2.00$ (E2), dash-dot-dotted: $\Gamma = 2.00$ (C) and dash-dotted: $\Gamma = 2.50$ (C). (*b*) Solid: $\Gamma = 0.775$ ($k_c = 3.260$) (E1), dotted: $\Gamma = 0.775$ ($k_c = 15.513$) (Q), dashed: $\Gamma = 1.036$ ($k_c = 2.781$) (E2), and dash-dotted: $\Gamma = 1.036$ ($k_c = 14.501$) (Q).

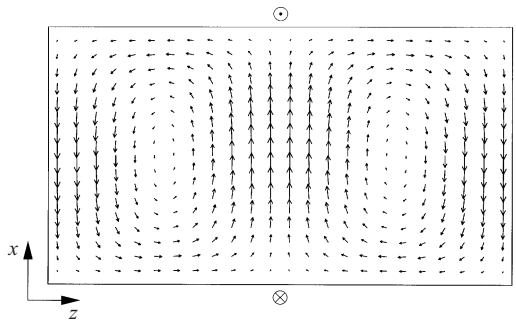


FIGURE 8. Neutral velocity field over one period in the z-direction for $\Gamma = 1.5$ in a cut at $y = 0$. Lengths are given to scale. The parameters are $Re_c = 191.9$ and $k_c = 2.353$.

stability owing to the self-induced strain (Widnall & Tsai 1977). For unbounded inviscid elliptical flow Pierrehumbert (1986) has shown numerically that the instability occurs on arbitrary small scales, and Bayly (1986) exactly solved the nonlinear equations to obtain the unstable modes in the form of plane waves whose wave vector rotates elliptically around the axis of the basic flow (see also Waleffe 1990). Recently, Kuhlmann *et al.* (1997) and Kuhlmann, Wanschura & Rath (1998) found that the elliptic instability mechanism is also operative in the two-sided lid-driven cavity where it leads to nonlinear three-dimensional flows with saturated amplitude. The present linear stability boundaries confirm these earlier results (cf. figure 2).

At the threshold, a stationary three-dimensional flow bifurcates supercritically (at least for $\Gamma = 1.96$, Kuhlmann *et al.* 1997) from the basic flow. The supercritical flow appears in the form of rectangular cells such that the spanwise velocity component w vanishes periodically on equally spaced planes separated by $\Delta z = \lambda_c/2$. The cellular character is visible from one period of the critical velocity field shown at $y = 0$ in figure 8. The wavenumber $k_c = 2\pi/\lambda_c$ at onset is given in figure 4. Note that the basic flow as well as the critical mode are point symmetric with respect to the centre of each cell at which $\boldsymbol{u} = \boldsymbol{u}_0 = 0$. Remarkably, the nonlinear three-dimensional flow also preserves this symmetry (Blohm & Kuhlmann 2002).

https://doi.org/10.1017/S0022112002007917 Published online by Cambridge University Press

https://doi.org/10.1017/S0022112002007917 Published online by Cambridge University Press

Aspect ratio	$\Gamma = 0.20$		$\Gamma = 0.90$		$\Gamma = 1.50$		$\Gamma = 2.17$		$\Gamma = 2.50$	
Reynolds number	$Re_c = 577.8$		$Re_c = 642.7$		$Re_c = 191.9$		$Re_c = 299.3$		$Re_c = 334.3$	
Type	E1		Q		E2		E3		C	
Production term	$\int I_i \,\mathrm{d}V$	$\int I_i' \,\mathrm{d}V$	$\int I_i \,\mathrm{d}V$	$\int I_i' \,\mathrm{d}V$	$\int I_i \,\mathrm{d}V$	$\int I_i' \,\mathrm{d}V$	$\int I_i \,\mathrm{d}V$	$\int I_i' \,\mathrm{d}V$	$\int I_i \,\mathrm{d}V$	$\int I_i' \,\mathrm{d}V$
$i = 1$	0.013	0.098	0.122	0.261	−0.454	0.033	−0.142	0.213	0.492	−0.043
2	−0.059	0.750	0.531	0.460	1.404	0.885	1.160	0.584	−0.409	0.714
3	0.982	0.004	−0.047	0.121	−0.190	−0.039	−0.144	−0.017	0.757	0.121
4	0.066	0.150	0.400	0.163	0.242	0.123	0.128	0.223	0.166	0.214

TABLE 2. Normalized energy production terms for several aspect ratios.

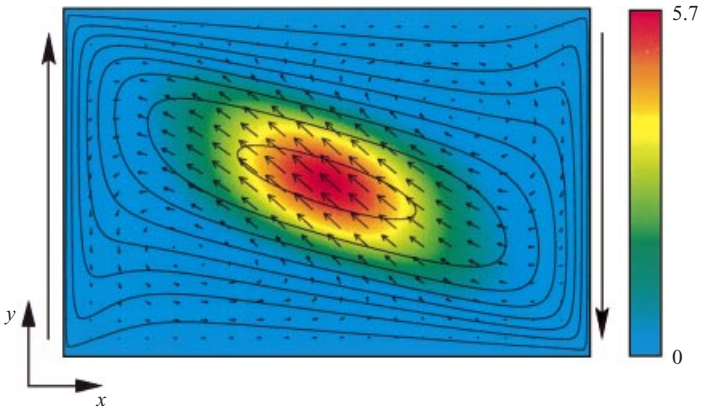


FIGURE 9. Basic-state streamlines (full lines) for $\Gamma = 1.5$ at criticality ($Re = Re_c = 191.9$) together with the local production I_2 (colour) and the critical velocity field (arrows) in the plane in which $w = 0$. In this plane I_2 takes its maximum value.

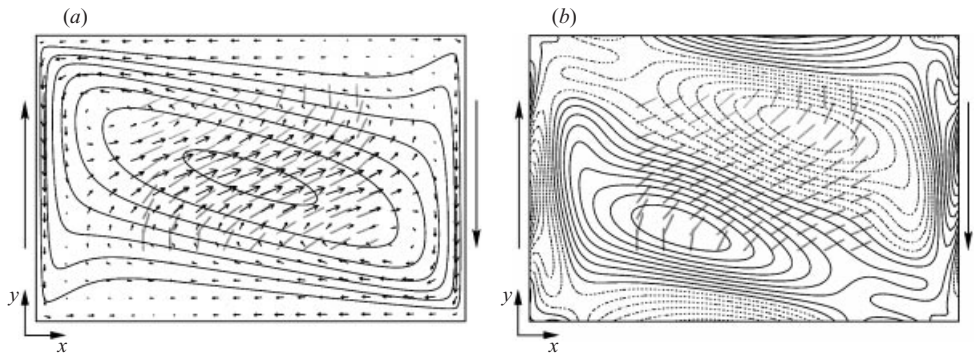


FIGURE 10. (*a*) Vorticity of the neutral mode (arrows) in a plane $z = \text{const.}$ through the centre of a convection cell. The contour lines are streamlines of the basic flow and the grey bars indicate the direction of the principal axis of strain of the basic flow. (*b*) Isolines of the z-component of the perturbation vorticity on the cell boundaries (where $w = 0$) shown together with the principal strain direction of the basic flow in the centre of the figure. The parameters for both (*a*) and (*b*) are $\Gamma = 1.5$, $Re = Re_c = 191.9$.

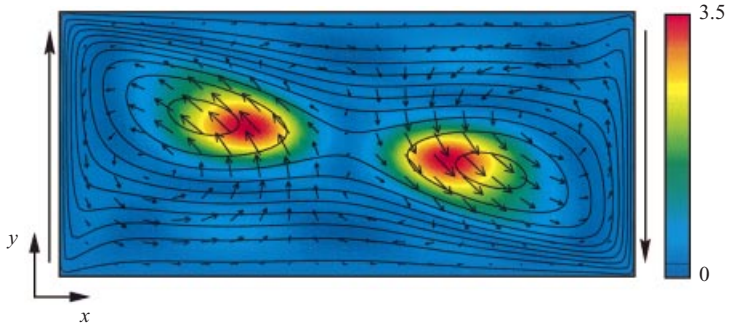


FIGURE 11. Basic-state streamlines (full lines) for $\Gamma = 2.17$ at criticality for the branch E3 ($Re = Re_c = 299.3$) together with the local production I_2 (colour) and the critical velocity field (arrows) in the plane in which $w = 0$. I_2 takes its maximum value in this plane.

https://doi.org/10.1017/S0022112002007917 Published online by Cambridge University Press

As a representative example, the elliptic base flow, the neutral velocity field, and the local energy transfer rate I_2 (cf. table 2) are shown in figure 9 on the cell boundary, i.e. in a plane in which $w = 0$. The aspect ratio $\Gamma = 1.5$ is near the minimum of the instability branch which occurs at $\Gamma_{\mathrm{E2,min}} = 1.428 \pm 0.001$, $Re_{\mathrm{E2,min}} = 189.8 \pm 1.1$, and $k_{\mathrm{E2,min}} = 2.406 \pm 0.001$.

Not only the elliptical shape of the streamlines of the basic flow and an energy transfer rate $\sum_i I_i$ which takes a maximum in the centre of the vortex indicate that the instability is of elliptic type. This conclusion is also supported by the structure of the critical mode in planes of constant z through the centre of the cells (offset by $\Delta z = \lambda_c/4$ from the cell boundary shown in figure 9). In these planes (an example is shown in figure 10*a*) the vorticity vector in the centre of each convection cell is coplanar to the (x, y)-plane and it is directed parallel or (alternatingly) anti-parallel to the principal strain axis. Such a behaviour is typical for the critical mode of the elliptic instability (Waleffe 1990). Another indicator of the elliptic instability is provided by the perturbation vorticity on the cell boundary (figure 10*b*). The z-component of the perturbation vorticity takes extrema which are located approximately on the main strain axis through centre of the basic-state vortex.

For large aspect ratios the topology of the basic flow changes smoothly along the linear stability curve. When the distance between the moving walls becomes larger, the strain in the centre of the cavity will eventually dominate the local rate of rotation and the elliptic stagnation point transforms into a hyperbolic stagnation point. On the critical curve, this happens at $\Gamma = 1.58 \pm 0.01$, $Re = 197.8 \pm 2.1$, $k = 2.307 \pm 0.006$. The smooth behaviour of the critical curve in this point and the continuous variation of the local energy-production rates indicate that the instability mechanism does not change. In fact, as was first shown by Kuhlmann *et al.* (1997) for $\Gamma = 1.96$, the region of maximum amplification remains in the centre of the cavity for this branch of instability and it is peaked at the hyperbolic stagnation point, even though two small recirculation regions exist in the basic flow, both being embedded in a globally circulating stream.

For even larger aspect ratios the critical curve E2 intersects with another critical curve E3 which is bounding the range of linear stability from below (figure 5). Since the neutral Reynolds numbers do not differ much, the basic flow is nearly identical for both instabilities. The critical modes, however, are quite different. The local energy production I_2 for the instability E3 exhibits two equal maxima (figure 11), each maximum being associated with one of the elliptical (to lowest order) vortices that make the characteristic cat's-eye pattern of the basic flow. As can be seen from figures 11 and 12 the critical mode now consists of a double row of cells. From the features of the critical mode, it is obvious that the instability is again of elliptical type. As can be seen from figure 13 the vorticity midway between the cell boundaries now has two local extrema, anti-parallel oriented, and both approximately aligned with the local axis of principal strain of the basic flow.

The appearance of the wedge-shaped tongue of linear stability between the critical curves E2 and E3 can be understood in terms of the basic-flow properties for constant Γ. When the Reynolds number is large, the wall jets emerging from both downstream corners of the moving walls are strong and they are comparatively thin (Kuhlmann *et al.* 1997). In this situation the basic-state streamlines in the centre of the cavity are elliptical and the flow is unstable to the mode E2 centred in the elliptic vortex. On a reduction of the Reynolds number the wall jets, and hence the elliptic vortex, become weaker so that the mode E2 is stabilized. In addition, the basic flow topology changes for decreasing Re. The closed streamlines in the centre of the cavity transform into a

https://doi.org/10.1017/S0022112002007917 Published online by Cambridge University Press

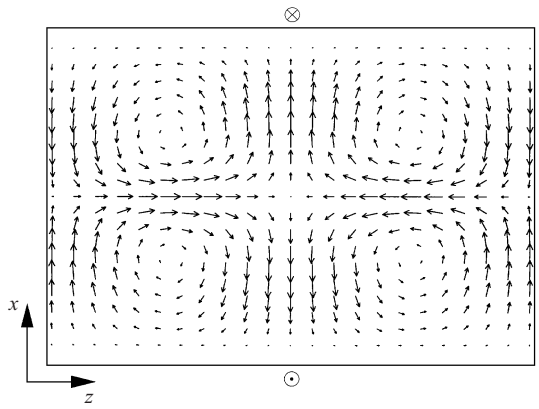


FIGURE 12. Critical velocity field for $\Gamma = 2.17$ in the plane $y = 0$ showing the double row of cells for the instability branch E3. The parameters are $Re_c = 299.3$ and $k_c = 2.024$.

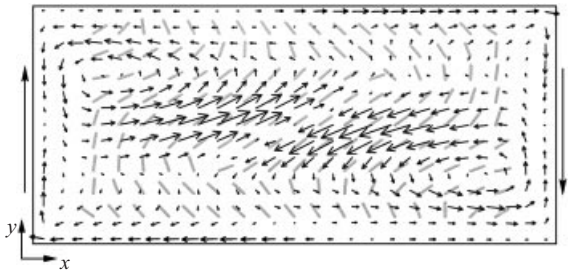


FIGURE 13. Vorticity of the critical mode (arrows) on the E3 branch for $\Gamma = 2.17$ in a plane $z = \text{const.}$ through the centres of two neighbouring cells. The grey bars indicate the direction of the principal axis of strain of the basic flow. The parameters are $Re_c = 299.3$ and $k_c = 2.024$.

hyperbolic stagnation-point flow and two embedded vortices are created in the centre at $x = y = 0$. These vortices grow stronger and are displaced towards the moving walls on a further decrease of Re. As the existence boundary of the strongly merged vortex flow is approached from above, the basic flow changes rapidly. In particular, the strengthening of the two embedded vortices is sufficient to enable the linear instability E3 to develop for decreasing Re in a small range of Reynolds numbers just before the basic flow breaks down.

For small aspect ratios, $\Gamma \downarrow (\approx 1)$, the strain in the centre of the cavity diminishes, because the streamlines become more circular. In fact, the flow in the centre of a cavity with $\Gamma = 1$ would be approximately in solid body rotation if the Reynolds number were large enough (Batchelor 1956). Hence, the elliptic instability process is suppressed, giving rise to a strong increase of the neutral E2 curve visible in figure 4. In this situation, however, a different instability mechanism takes over and leads to the instability Q (see § 3.5).

3.2. *Elliptic instability for* $\Gamma < 0.775$ (*E1*)

As the aspect ratio tends to zero the basic flow in the centre of the cavity far away from the rigid stationary walls at $y = \pm 1/2$ approaches plane Couette flow. This flow is linearly stable (see e.g. Drazin & Reid 1981). Any linear instability, therefore, must be due to the return flow near the rigid walls. In fact, the return flow is linearly unstable.

https://doi.org/10.1017/S0022112002007917 Published online by Cambridge University Press

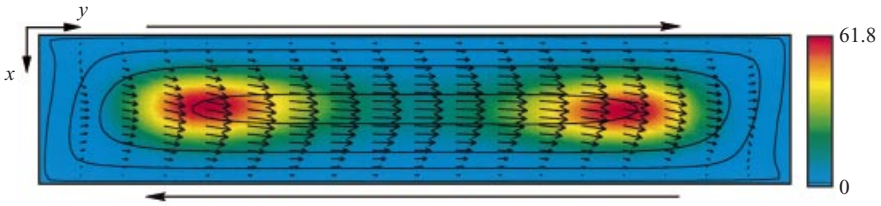


FIGURE 14. Basic-state streamlines for $\Gamma = 0.20$ and $Re_c = 577.8$, critical mode (arrows), and local production rate I_3 (colour) in a plane $z = \text{const.}$ in which I_3 takes its absolute maximum.

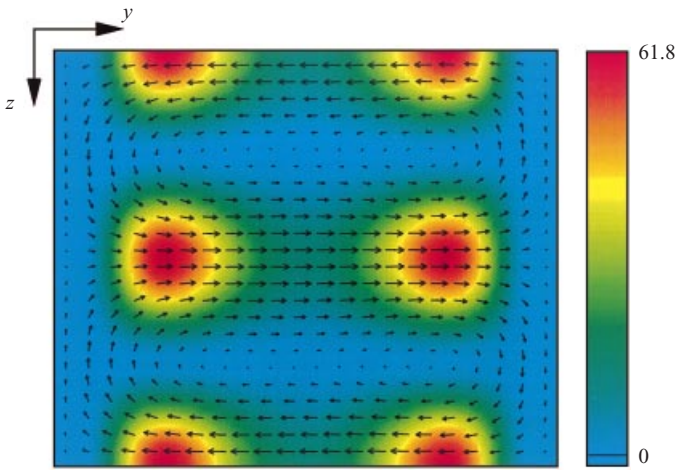


FIGURE 15. Neutral velocity field (arrows) over one wavelength shown at $x = 0$ for $\Gamma = 0.20$ and $Re_c = 577.8$. The production term I_3 is indicated in colour.

As an example we consider $\Gamma = 0.20$. The energy budget of the critical mode (table 2) indicates that nearly all energy is supplied by the basic flow through the term I_3. This term is equivalent to I_2' in the bulk of the cavity. The spatial distribution of I_3, given in figure 14, shows that the production of energy is strongly localized midway between the two moving walls and near the end regions where the basic-state streamlines are sharply curved. In the bulk, practically no energy is transferred from the basic to the perturbation flow, as expected. This is because the production terms I_1, I_2 and I_4 become zero in plane shear flow, and because both the u- and the v-components of the disturbance flow are required to extract energy from the basic flow via I_3. The cross-stream component u, however, decays rapidly away from the endwalls at $y = \pm 1/2$, whereas the fluctuation v is amplified by the underlying basic shear with a gradient $\partial v_0/\partial x = 2Re_c/\Gamma = 1156/0.20 = 5780$. Therefore, u can be expected to be three to four orders of magnitude smaller than v in the bulk, even if both velocity components are of the same order of magnitude in the turning zones. Hence, the neutral mode in the bulk consists of streaks of streamwise perturbation velocity v. The streaks arise in pairs and are seen in the velocity field of the neutral mode shown in figure 15 for $x = 0$. Since the cross-stream velocity component u is small even in the turning zones, the streaks turn near $y = \pm 1/2$ via a non-zero velocity component w. The streaks are only slightly asymmetric with respect to $x = 0$. A cross-section through a pair of streaks (one wavelength of the critical mode) in the plane $y = 0$ is shown in figure 16. Only in this plane are the isolines of v exactly symmetric with respect to $x = 0$.

https://doi.org/10.1017/S0022112002007917 Published online by Cambridge University Press

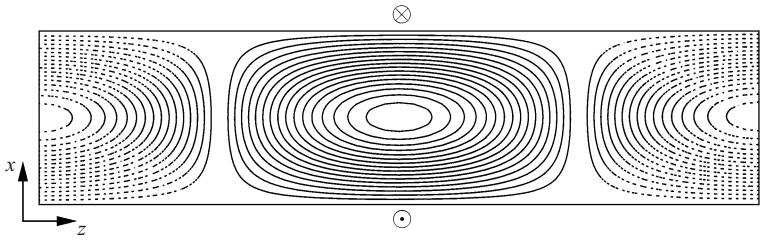


FIGURE 16. Isolines of the critical velocity component v in the plane $y = 0$ for $\Gamma = 0.20$ and $Re_c = 577.8$.

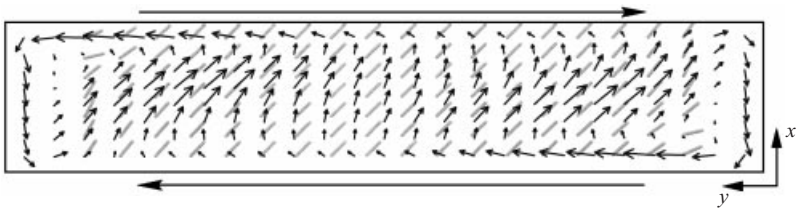


FIGURE 17. Critical vorticity field (arrows) and principal strain direction (grey lines) in a plane $z = \text{const.}$ midway between two streaks for $\Gamma = 0.20$ and $Re_c = 577.8$.

Since the basic flows for $\Gamma = 1.5$ (E2) and for $\Gamma = 1.5^{-1}$ (E1) are similar and characterized by elliptical streamlines in the centre (the major difference is due to the exchange of the minor and major semi-axes) it is reasonable to expect a similar instability mechanism in both cases. As in § 3.1, one can argue that the branch E1 is an elliptic instability. In particular, the region of maximum energy transfer is located in the centre of the elliptical vortex if the aspect ratio is not too small. When Γ decreases the elliptical streamlines are stretched out and become nearly parallel in the central part of the cavity. Moreover, the central energy production peak splits into two well-separated peaks (figures 14 and 15). The neutral mode, however, extends over the whole cavity (figure 15) owing to the streak-producing shear flow. On a further decrease of Γ one might expect the neutral mode to separate into two nearly independent perturbation flows located near each of the endwalls. This mode separation could not be investigated here, because the streaks reach far into the bulk. It is worth noting that even for small Γ the instability is of elliptic type. This conclusion is supported by figure 17, showing the alignment of the perturbation vorticity with the principle stain axis in the regions of maximum energy transfer. This behaviour underlines the importance of vortex stretching in the instability process (Waleffe 1990).

The question arises of whether the critical Reynolds number remains finite as $\Gamma \to 0$. In this limit the Reynolds number defined in (2.4) would tend to infinity for any arbitrary small velocity V. Moreover, since the separation d of the moving walls is the only available length scale, it is appropriate to use the Reynolds number and wavenumber for plane shear flows, $Re^* = Re\,\Gamma$ and $k_c^* = k_c\Gamma$, respectively, when $h \gg d$. In figure 18 we have plotted the critical Reynolds number Re_c^* and the critical wavenumber k_c^* as functions of Γ. Since the number of grid points required for small Γ increases, and because the minimum of $Re_n(k)$ becomes very shallow, we have terminated our calculations at $\Gamma = 0.10$. From the present result it is anticipated that the critical Reynolds number will remain finite with a value $Re_c^*(\Gamma \to 0) \approx 160$ and $k_c^*(\Gamma \to 0) \approx 1.5$.

https://doi.org/10.1017/S0022112002007917 Published online by Cambridge University Press

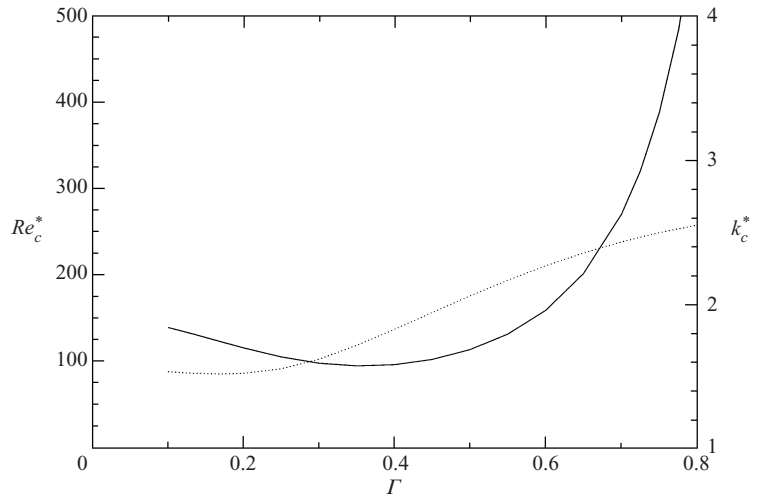


FIGURE 18. Critical Reynolds number Re_c^* (full line) and critical wavenumber k_c^* (dotted line) for small values of Γ.

3.3. *Comparison of the elliptic instability in bounded and unbounded domains*

The elliptic instability for unbounded linear viscous flows has been treated by Landman & Saffman (1987) and Haj-Hariri & Homsy (1997). For a qualitative comparison with Landman & Saffman (1987) we consider the streamline eccentricity

$$\beta = \frac{\epsilon}{\gamma}, \tag{3.1}$$

where ϵ is the rate of strain and $\gamma = \omega_0/2$ the rotation rate given by half the vorticity. The streamline eccentricity β in the centre of the cavity is shown in figure 19 as a function of the aspect ratio Γ for the neutral Reynolds number $Re_n(\Gamma)$ along the two branches of the elliptic instability E1 and E2 which are connected with each other near $\Gamma \approx 1$ (not visible on the scale of figure 4). The eccentricity of the streamlines has a minimum at $\Gamma \approx 0.93$ ($Re_n \approx 2436$). For this aspect ratio the neutral curve connecting E1 and E2 has a sharp maximum and instead of the elliptic-instability mode a different mode (Q) is critical.

In order to compare the present elliptic instability in a finite, wall-bounded domain with the result for unbounded viscous elliptic flow we follow Landman & Saffman (1987) and consider the range of flow instability in the (β, E_γ)-plane, where

$$E_\gamma = \frac{2\pi}{\cos^2\theta}\frac{k_0^2}{\gamma} \tag{3.2}$$

is the Ekman number based on the vorticity. For the unbounded system $k_0 = |\boldsymbol{k}_0|$ is the absolute value of the critical wave vector and θ the angle between $\boldsymbol{k}_0$ and the basic vorticity (z-axis). A comparison of the lid-driven-cavity flow with the unbounded elliptical flow is made difficult by the fact that the angle θ cannot unambiguously be determined here. For a qualitative comparison, therefore, we set $k_0 = k_c$ and $\theta = 0$. Figure 20 shows that the Ekman number for the neutrally stable cavity flow evaluated in this manner is smaller than the corresponding one for the critical unbounded elliptic flow. Hence, the unbounded flow is more unstable for $\beta \lesssim 1$ than the cavity flow with the same streamline eccentricity in the centre. Only for $\beta \gtrsim 1$ and $\Gamma \geqslant 0.93$ is the cavity flow more unstable than the unbounded flow, which is linearly stable for

https://doi.org/10.1017/S0022112002007917 Published online by Cambridge University Press

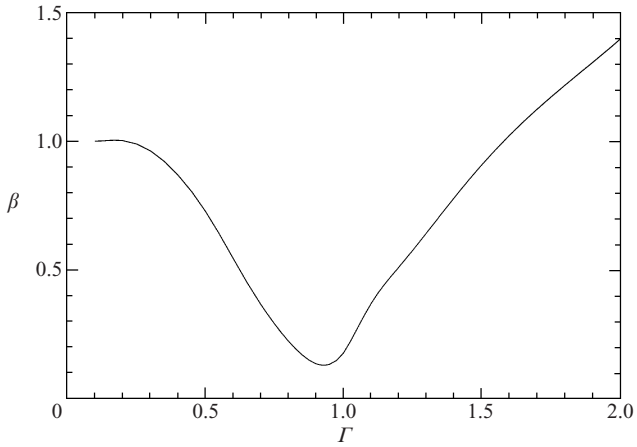


FIGURE 19. Streamline eccentricity parameter β evaluated in the centre of the cavity ($x = y = 0$) and along the neutral curve connecting the branches E1 and E2 (figure 4) as function of the aspect ratio Γ.

$\beta = 1$ (plane Couette flow). This is due to the local production of energy which is no longer centred in the cavity when the aspect ratio becomes extreme ($\Gamma \to (0, \infty)$). To better take into account the effect of θ we evaluated θ from the critical mode of the unbounded elliptical flow (figure 3 of Landman & Saffman 1987) and used this value to calculate the Ekman number (3.2) for the neutrally stable cavity flow. The aspect ratios were selected to fit the values of β for which θ was provided by Landman & Saffman (1987). This significantly improves the result (see figure 20) and both curves are now similar with a maximum near $\beta \approx 0.5$. Yet, the critical Ekman number for the lid-driven cavity is smaller by approximately a factor of two compared to the critical Ekman number for unbounded elliptical flow, i.e. the cavity flow is more stable than the unbounded flow. The qualitative agreement of the linear stability boundaries of the bounded and unbounded flow is another indication of the elliptic instability mechanism in the lid-driven cavity along the branches E1 and E2. We conclude that the *boundary effects*, which are responsible for driving as well as for dissipation of the flows in the cavity, act to stabilize the flow near the centre of the cavity where the streamlines are approximately elliptical in a range of Γ.

3.4. *Centrifugal instability for* $\Gamma > 1.951$ (*C*)

When the aspect ratio is larger than $\Gamma = 1.951$ the basic two-vortex flow becomes unstable along the critical curve denoted C in figure 4. The instability C of the two-vortex state has a long wavelength. A typical critical mode in the (x, z)-plane is shown in figure 21 for $y = 0.25$. As can be seen from figure 22(a) the mode appears in the form of two counter-rotating vortices primarily aligned in the z-direction, slightly offset from the basic co-rotating vortices and towards the centre of the cavity. The finite but small-amplitude flow would thus appear as two vortices whose diameters in the x-direction alternatingly shrink and expand along the axes of the basic vortices. These results are in agreement with those of Kuhlmann *et al.* (1997).

To understand the physical instability mechanism of the instability C the major energy-transfer rates for $\Gamma = 2.5$ are given in table 2. While three terms are significant in the Cartesian coordinate system (2.10), one net stabilizing and two net destabilizing ones, only the single term I_2' is significant and destabilizing when using

https://doi.org/10.1017/S0022112002007917 Published online by Cambridge University Press

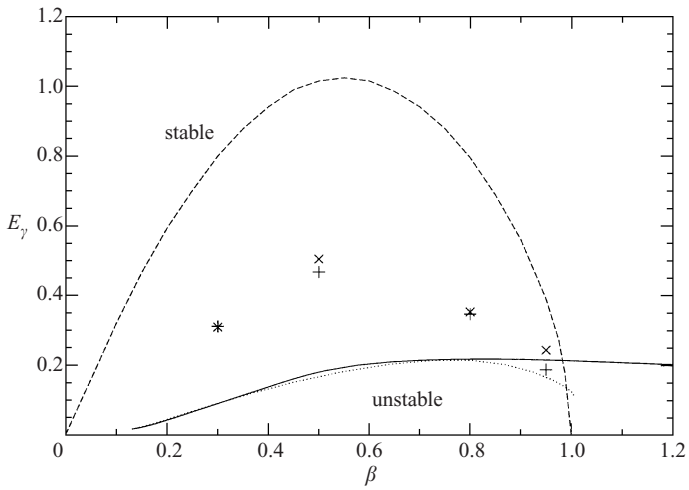


FIGURE 20. Ekman number E_γ as function of the streamline-eccentricity parameter β evaluated in the centre of the cavity for the neutrally stable basic flow. Solid and dotted lines denote results for $\Gamma > 0.93$ (E2) and $\Gamma < 0.93$ (E1), respectively. The symbols $\times$ and $+$ indicate Ekman numbers for the neutrally stable flow at selected aspect ratios with $\Gamma > 0.93$ (E2) and $\Gamma < 0.93$ (E1), respectively, when the angle θ between the wave vector and the z-axis is taken into account as given in Landman & Saffman (1987). The dashed line is the Ekman number below which the unbounded elliptical flow is linearly unstable according to Landman & Saffman (1987).

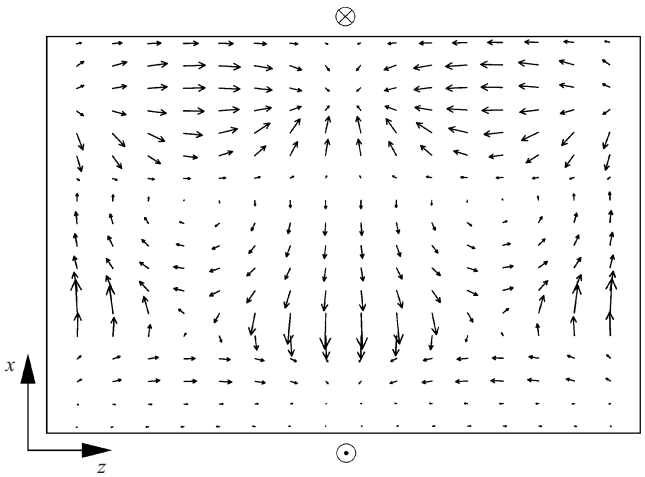


FIGURE 21. Critical velocity field for the instability C projected onto the plane $y = 0.25$ for $\Gamma = 2.5$ and $Re_c = 334.3$.

the longitudinal/transversal decomposition of the energy-transfer rates (2.11). The total local production rate $\sum_i I_i'$ (I_2' dominates) is shown in figure 22(a).

Due to inertia, the fluid emerging from the downstream corners of the moving walls could be expected to flow nearly parallel to the rigid walls into the cavity (compare also Pan & Acrivos 1967). In fact, this happens for the strongly merged vortex flow (Kuhlmann *et al.* 1997; Albensoeder *et al.* 2001*a*). However, in the present two-vortex flow, continuity and the suction by the corner upstream of each moving wall force the fluid into two nearly circular vortices. Owing to the stationary rigid walls the

https://doi.org/10.1017/S0022112002007917 Published online by Cambridge University Press

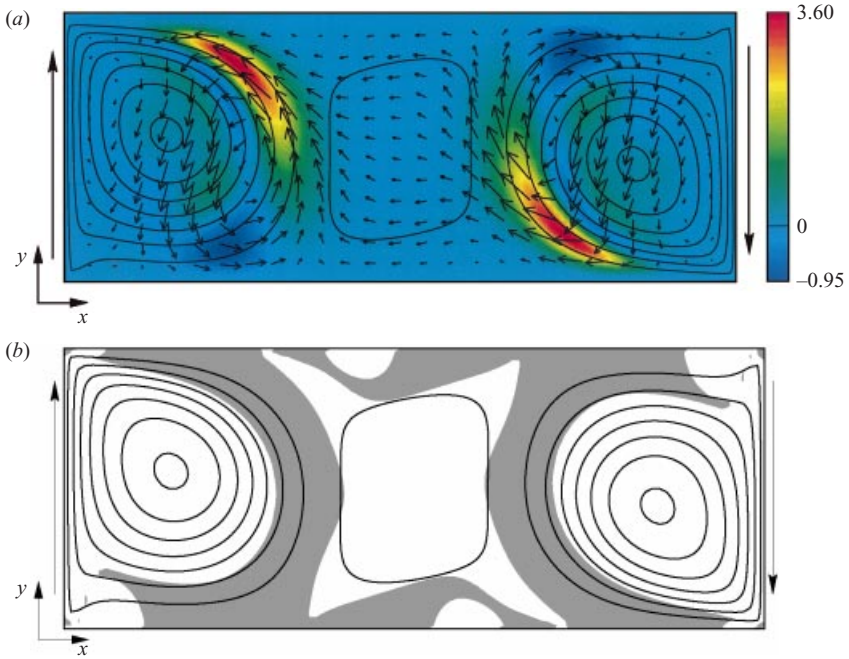


FIGURE 22. (*a*) Basic state (streamlines), critical velocity fields (arrows), and the total local production $\sum_i I_i$ (colour) for $\Gamma = 2.5$ and $Re_c = 334.3$. Shown is a cut at constant z where the local production takes its absolute maximum. (*b*) Basic-state streamlines for the same parameters as (*a*) together with regions for which $|\boldsymbol{u}_0|\omega_0/R < 0$ (grey-shaded).

velocity gradient perpendicular to the convex streamlines and radially outward from the centre of the vortex is negative near the outermost streamlines and near the region where the flow separates from the rigid walls. This is evident from the density of the streamlines in the regions of maximum production (red in figure 22*a*). These local flow conditions are favourable for a centrifugal instability. While no rigorous criterion exists for a centrifugal instability in general viscous two-dimensional flows, Bayly (1988) proved that a two-dimensional inviscid flow is centrifugally unstable if the streamlines are closed convex curves in some region of the flow and the magnitude of the circulation decreases outward. An equivalent form of this criterion has recently been given by Sipp & Jacquin (2000). Accordingly, the inviscid flow is centrifugally unstable if

$$\frac{|\boldsymbol{u}_0|\omega_0}{R} < 0 \tag{3.3}$$

on a whole streamline ψ_0, where R is the local radius of curvature of the streamline and ω_0 the basic-state vorticity. We have evaluated (3.3) for the neutrally stable viscous flow in a cavity with $\Gamma = 2.5$. The result is shown in figure 22(*b*). Owing to the signs of the streamline curvature and the vorticity, (3.3) cannot hold near the moving walls. However, the criterion is satisfied in extended regions originating near the downstream corners of the moving walls and stretched along the outer streamlines of both vortices. We find that the total local energy transfer $\sum I_i'$ (I_2' dominates) is peaked and stretched parallel to the streamlines in just the region where (3.3) is satisfied (compare figure 22(*a*)). From these arguments we conclude that the instability is of centrifugal type. Only in the region of curved streamlines approaching

https://doi.org/10.1017/S0022112002007917 Published online by Cambridge University Press

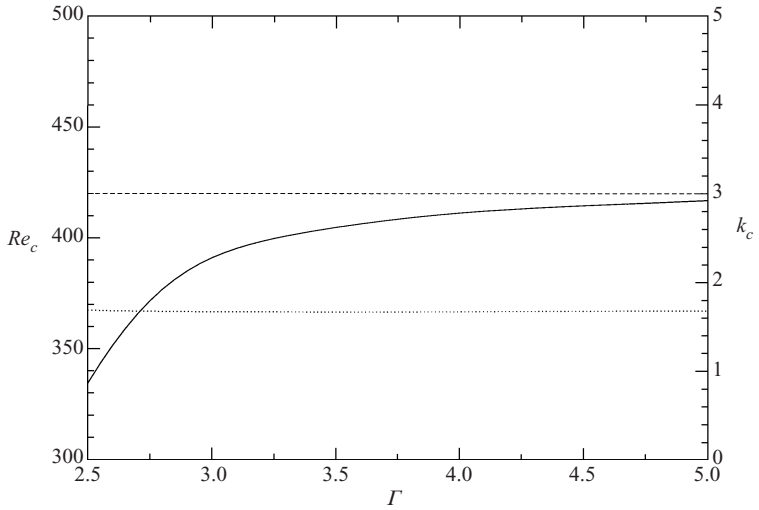


FIGURE 23. Critical Reynolds number (solid line) and wavenumber (dotted line) for large aspect ratios Γ. The approximate asymptotic value $Re_c(\Gamma \to \infty) \approx 420$ (Albensoeder *et al.* 2001*b*) is indicated as a dashed line.

the upstream corners of the moving walls is the production term I_2' negative, because the velocity field of the critical mode has a component parallel (anti-parallel) to the basic flow and in the direction of increasing (decreasing) basic-state momentum (see figure 2 of Albensoeder *et al.* 2001*b*).

When Γ is large, each moving wall drives its own primary vortex and a sequence of weak secondary Moffatt eddies (Moffatt 1964). Because the latter decay exponentially towards the interior, both main vortices become independent for $\Gamma \to \infty$. The extrapolated asymptotic critical Reynolds number and the critical wavenumber for $\Gamma \to \infty$ are found to coincide with the corresponding values for the single-lid-driven cavity (Albensoeder *et al.* 2001*b*). The asymptotic behaviour of the critical Reynolds number and wavenumber is shown in figure 23.

3.5. *Quadripolar instability for* $0.775 < \Gamma < 1.036$ (Q)

In the near-unity aspect-ratio range $0.775 < \Gamma < 1.036$ where the elliptic instability process is suppressed, because the dipolar strain field is very weak in the centre of the vortex (minimum of β in figure 19), another neutral mode becomes critical. Its critical wavelength $\lambda_c = 2\pi/k_c$ is much shorter than all other length scales. The basic-state stream function, the total local energy transfer, and the structure of the critical mode are shown in figure 24. As can be seen, there is practically no energy supply from the basic state in the vortex core. All energy production takes place near the outer streamlines, in particular near both corners downstream of the moving walls.

One might expect that the present instability is similar to the one in the classical one-sided lid-driven square cavity. In fact, the critical Reynolds and the critical wavenumbers are of comparable magnitude in both cases and both instabilities are stationary (Albensoeder *et al.* 2001*b*). Moreover, the locations of sizable energy transfer from the basic states are similar. The neutral modes, however, differ completely. While the critical mode in the classical cavity consists of localized Taylor–Görtler-like vortices, the critical flow in the present case does not consist of toroidal vortices whose vorticity is aligned with the basic-flow direction. In contrast, we find a critical mode consisting of four eddies within half a wavelength in z-direction. These eddies

https://doi.org/10.1017/S0022112002007917 Published online by Cambridge University Press

are located in the four corners of the cavity and they have a vorticity which is very well aligned with the direction of the strain (cf. figure 27 below), approximately in the direction of the bisection of the respective corner. The fluid motion can be inferred from figure 24 and figure 25 which show the critical mode in a spanwise plane at $y = 0$. Consider, for instance, the two streams at the bottom of figure 25, showing the midplane $y = 0$, which approach each other from the left- and the right-hand side ($x = \pm\Gamma/2$). The streams meet approximately in the centre of the cavity and split into two streams which leave the plane $y = 0$ in the positive and negative y-direction. These streams in the y-direction and near $x = 0$ approach the rigid walls at $y = \pm 1/2$ where they turn and flow back towards the centre of the cavity. This backflow is visible in figure 24 as the two streams coming from the top and from the bottom. Figure 24 shows that both colliding streams are approximately symmetrically deflected into two streams near $y = 0$ which are directed in the positive and negative x-direction towards the moving walls. These jets are also visible at mid-height in figure 25. In the vicinity of the moving walls the jets split and return towards the centre (top and bottom of figure 25). This closes the flow loop. The associated fluid motion is distinctly different from the Taylor–Görtler vortices (Albensoeder *et al.* 2001*b*).

3.6. *Comparison with the quadripolar instability of a strained Rankine vortex*

While the instability Q of the cavity flow does not appear to be related to the Taylor–Görtler instability, it exhibits all the features of the instability of a vortex in a quadripolar strain field. When a vortex of finite diameter is subject to an externally imposed quadripolar strain field the streamlines in the centre of the vortex are circular. Towards the periphery of the vortex, where the strain dominates, the streamlines are more distorted and approach a square shape in the case of a Rankine vortex. Eloy & Le Dizés (2001) investigated the instability of a Rankine vortex in a multipolar strain field, including the asymptotic influence of viscosity. For a quadripolar strain field they found the following features.

(*a*) When the Reynolds number is not too large the most unstable mode is stationary.

(*b*) The instability is due to a resonance of two Kelvin modes (Saffman 1992) with fundamental azimuthal wavenumbers $m = \pm 2$. Therefore, the perturbation mode is double periodic along a streamline.

(*c*) The instability arises in the limit of large axial wavenumbers k. Since high-wavenumber modes suffer high viscous damping, the critical Reynolds number will be larger than for comparable elliptic-flow instabilities.

(*d*) The mechanism of instability is dominated by the stretching of perturbation vorticity by the basic flow such that the perturbation vorticity becomes aligned in the stretching direction. The perturbations are localized in the region of maximum stretching rate which occurs near the edge of the vortex core where the streamline curvature is large.

The basic cavity flow exhibits similar streamlines to the Rankine vortex in quadripolar strain, except for details near the downstream corners of the moving walls. To compare the present closed flow with the instability of an unbounded, weakly strained Rankine vortex we write the critical conditions found by Eloy & Le Dizès (2001) (their figure 10) in the form

$$Re_c \approx \frac{1}{7.5 \times 10^{-4}} \frac{1}{\epsilon_4^2} \quad \text{and} \quad k_c \approx \frac{25}{\sqrt{\epsilon_4}}, \tag{3.4}$$

https://doi.org/10.1017/S0022112002007917 Published online by Cambridge University Press

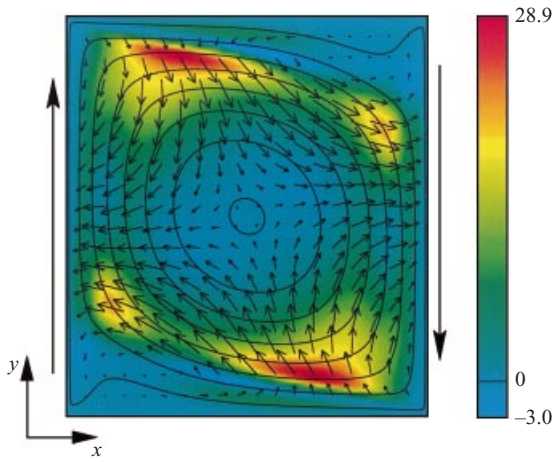


FIGURE 24. Basic state streamlines (full lines), neutral mode (arrows), and the total local production $\sum_i I_i$ (colour) for $\Gamma = 0.9$ and $Re_c = 642.7$. Shown is a plane $z = \text{const.}$ (see figure 25) in which the total local production takes its absolute maximum.

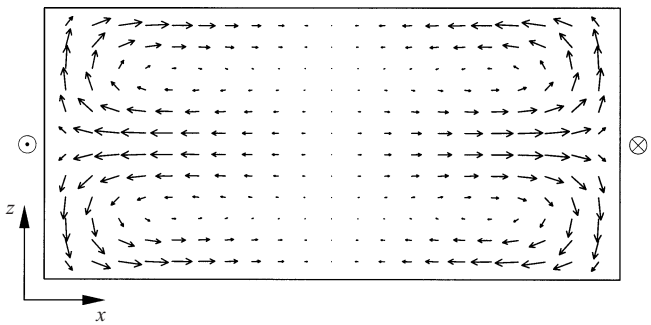


FIGURE 25. Critical mode for $\Gamma = 0.9$ and $Re_c = 642.7$ in the plane $y = 0$.

where ϵ_4 is the strength parameter of the quadripolar strain. The estimate (3.4) is obtained by identifying the scales $h = a$ and $V = a\Omega$, with a being the radius of the Rankine vortex and Ω its rotation rate. To determine the magnitude of the quadripolar strain the streamlines of the cavity flow are fitted to

$$\psi(r,\theta) = \psi(0,0) + cRe\left[\frac{r^2}{2} + \epsilon_2\frac{r^2}{2}\sin(2\theta+\theta_2) + \epsilon_4\frac{r^4}{4}\sin(4\theta+\theta_4)\right], \qquad (3.5)$$

using polar coordinates (r,θ) centred at $x = y = 0$. In this form of the stream function the dipolar and quadripolar strain-rate parameters ϵ_2 and ϵ_4 are identical to those in Eloy & Le Dizès (2001). The free parameters are ϵ_2, ϵ_4, the phases θ_2 and θ_4, and the 'vortex-strength' parameter c.

We find that all the fitting parameters are almost constant in the vortex core, at least for the range of Γ where the instability Q is significant. As an example ϵ_2, ϵ_4 and c are shown in figure 26(a) for $\Gamma = 0.9$ and $Re = Re_c = 642.7$. Since (3.5) is the general asymptotic form of a potential flow without singularities, the result shows that the vortex core is nearly inviscid. For $r > 0.4$ viscous wall effects become important. In figure 26(b) the ratio of the quadripolar to the dipolar strain parameters is plotted as function of the aspect ratio Γ. It shows that the quadripolar strain is dominant and

https://doi.org/10.1017/S0022112002007917 Published online by Cambridge University Press

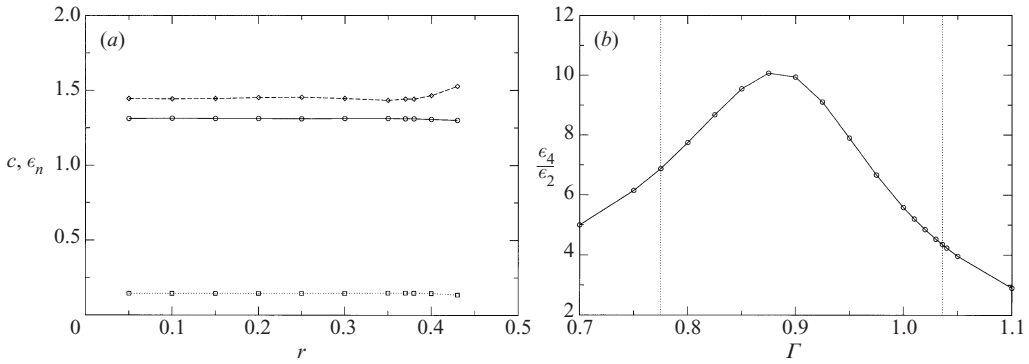


FIGURE 26. (*a*) Fitted values of c (○), ϵ_2 (□) and ϵ_4 (◇) as functions of the radius r. The parameters are $Re = Re_c = 642.7$ and $\Gamma = 0.9$. (*b*) The ratio ϵ_4/ϵ_2 as function of Γ for $r = 0.3$. The Reynolds number corresponds to the neutral value of the instability branch Q, $Re(\Gamma) = Re_c^{(Q)}(\Gamma)$. The dotted lines denote the limits for the quadripolar instability.

that ϵ_4/ϵ_2 takes a maximum within the region of Γ where the instability Q occurs. The strain rate parameters at this maximum are $\epsilon_2 \approx 0.15$ and $\epsilon_4 \approx 1.5$. Using the value $\epsilon_4(\Gamma = 0.9) \approx 1.5$ we obtain from (3.4) a prediction for the critical values,

$$Re_c \approx 590 \quad \text{and} \quad k_c \approx 20, \tag{3.6}$$

expected from the analysis of Eloy & Le Dizès (2001). These estimates are in surprisingly good agreement with the critical values for the cavity flow $Re_c = 642.7 \pm 1.7$ and $k_c = 14.89 \pm 0.03$.

The above consideration shows that the critical Reynolds numbers and wavenumbers are comparable for a quadripolarly strained Rankine vortex and the present cavity flow with $\Gamma = 0.9$. Also, the critical Reynolds numbers for the branch Q are higher than for the elliptic instability (cf. figure 4), similar to the stability properties of strained Rankine vortices (Eloy & Le Dizès 2001). Altogether, the cavity flow instability Q satisfies the characteristic features (*a–c*).

Finally, we consider the total local energy production in the plane $z = \text{const.}$ in which the production takes its maximum value. From figure 24 the local production has four maxima, not exactly on the bisection, but near the four corners of the cavity where the outer streamlines have the highest curvature. These are also the regions of high strain rate of the basic flow. The direction of the basic strain field is shown in figure 27. A comparison with figure 24 clearly proves the good correlation of the perturbation vorticity vector and the basic-state strain direction. The vorticity is very large near the four corners of the cavity, corresponding to the four edges of the outer basic-state streamlines. This observation qualitatively validates feature (*d*).

The foregoing discussion has shown that the present instability Q for nearly unit aspect ratios exhibits essentially the same properties as the instability of a Rankine vortex in a quadripolar strain field. We conclude, therefore, that the instability found here is the first reported manifestation of the quadripolar instability in a bounded flow.

4. Conclusion

The flow in rectangular cavities driven by opposing wall motion has been investigated in the limit of infinite span. Using a finite-volume technique and the normal

https://doi.org/10.1017/S0022112002007917 Published online by Cambridge University Press

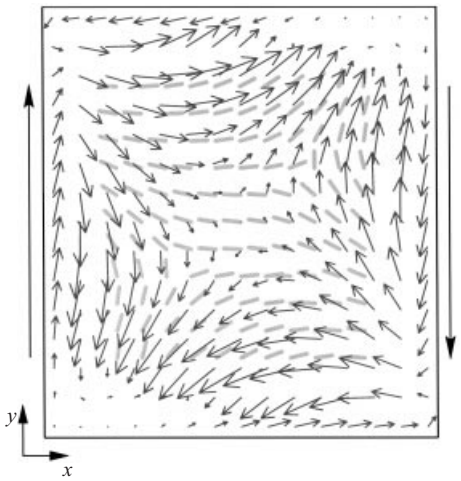


FIGURE 27. Direction of the basic-state strain field (grey lines) and vorticity of the critical mode (arrows) for $\Gamma = 0.9$ and $Re = Re_c = 642.7$.

modes in spanwise direction the linear stability of various two-dimensional flows has been calculated.

If the separation of the moving walls is sufficiently large compared to the distance between the stationary rigid walls the basic flow consists of two well-separated vortices, each driven by one of the moving lids. This type of flow becomes centrifugally unstable in three dimensions to the same type of stationary perturbations as in the classical one-sided lid-driven cavity (Albensoeder *et al.* 2001*b*). The extrapolated critical Reynolds numbers and wavenumbers for $\Gamma \to \infty$ are the same.

When the two moving walls are closer the two-dimensional vortices partly merge and typically form an elliptic vortex (strongly merged vortex flow). This vortex flow is subject to a strong dipolar strain. The straining motion gives rise to an elliptic instability which is caused by a resonance between two Kelvin waves with fundamental azimuthal wavenumber $m = \pm 1$.

For aspect ratios near unity, the basic-state vortex is only weakly strained in its centre, but it is strained in four directions near the four cavity corners. This quadripolar strain is a result of the cavity geometry and the motion of the two opposing walls. By comparing the characteristic properties of the basic flow and the most unstable mode with the instability of a quadripolar-strained Rankine vortex (Eloy & Le Dizès 2001) we conclude that both instabilities are caused by the same mechanism, i.e. a resonance between two Kelvin waves of azimuthal wavenumber $m = \pm 2$.

If the separation of the moving walls is significantly smaller than the stationary wall distance the streamlines of the basic flow are again elliptic and the basic flow suffers an elliptic instability. For shallow cavities with $\Gamma \ll 1$ the elliptic instability arises in both symmetric end zones where the basic flow turns. The bulk flow, being approximately a plane-Couette flow, cannot provide any energy to the perturbations, but the critical mode penetrates far into the bulk from the end zones in the form of wide stationary streaks.

This work has been supported by DFG under grant numbers Ku896/5-2 and Ku896/8-1.

https://doi.org/10.1017/S0022112002007917 Published online by Cambridge University Press

REFERENCES

Albensoeder, S. & Kuhlmann, H. C. 2002 Three-dimensional instability of two counter-rotating vortices in a rectangular cavity driven by parallel wall motion. *Eur. J. Mech.* B/*Fluids* (to appear).

Albensoeder, S., Kuhlmann, H. C. & Rath, H. J. 2001*a* Multiplicity of steady two-dimensional flows in two-sided lid-driven cavities. *Theor. Comp. Fluid Dyn.* **14**, 223–241.

Albensoeder, S., Kuhlmann, H. C. & Rath, H. J. 2001*b* Three-dimensional centrifugal-flow instabilities in the lid-driven cavity problem. *Phys. Fluids* **13**, 121–135.

Alleborn, N., Raszillier, H. & Durst, F. 1999 Lid-driven cavity with heat and mass transport. *Intl J. Heat Mass Transfer* **42**, 833–853.

Batchelor, G. K. 1956 On steady laminar flow with closed streamlines at large Reynolds numbers. *J. Fluid Mech.* **1**, 177–190.

Bayly, B. J. 1986 Three-dimensional instability of elliptical flow. *Phys. Rev. Lett.* **57**, 2160–2163.

Bayly, B. J. 1988 Three-dimensional centrifugal-type instabilities in inviscid two-dimensional flows. *Phys. Fluids* **31**, 56–64.

Bayly, B. J., Orszag, S. A. & Herbert, T. 1988 Instability mechanisms in shear flow transition. *Annu. Rev. Fluid Mech.* **20**, 359–391.

Benjamin, D. F., Anderson, T. J. & Scriven, L. E. 1995 Multiple roll systems: steady state operation. *AIChE J.* **41**, 1045–1060.

Blohm, C., Albensoeder, S., Kuhlmann, H. C., Broda, M. & Rath, H. J. 2001 The two-sided lid-driven cavity: aspect-ratio dependence of the flow stability. *Z. Angew. Math. Mech.* **81** (Supplement 3), 781–782.

Blohm, C. & Kuhlmann, H. C. 2002 The two-sided lid-driven cavity: experiments on stationary and time-dependent flows. *J. Fluid Mech.* **450**, 69–95.

Botella, O. & Peyret, R. 1998 Benchmark spectral results on the lid-driven cavity flow. *Comput. Fluids* **27**, 421–433.

Ding, Y. & Kawahara, M. 1998 Linear stability of incompressible fluid flow in a cavity using finite element method. *Intl J. Num. Meth. Fluids* **27**, 139–157.

Ding, Y. & Kawahara, M. 1999 Three-dimensional linear stability analysis of incompressible viscous flows using the finite element method. *Intl J. Num. Meth. Fluids* **31**, 451–479.

Drazin, P. G. & Reid, W. H. 1981 *Hydrodynamic Stability*. Cambridge University Press.

Eloy, C. & Le Dizès, S. 2001 Stability of the Rankine vortex in a multipolar strain field. *Phys. Fluids* **13**, 660–676.

Ferziger, J. H. & Perić, M. 1996 *Computational Methods for Fluid Dynamics*. Springer.

Gaskell, P. H., Gürcan, F., Savage, M. D. & Thompson, H. M. 1998 Stokes flow in a double-lid-driven cavity with free surface side walls. *Proc. Inst. Mech. Engrs* **212** (Part C), 387–403.

Gaskell, P. H., Summers, J. L., Thompson, H. M. & Savage, M. D. 1996 Creeping flow analyses of free surface cavity flows. *Theor. Comput. Fluid Dyn.* **8**, 415–433.

Ghia, U., Ghia, K. N. & Shin, C. T. 1982 High-Re solutions for incompressible flow using the Navier-Stokes equations and a multigrid method. *J. Comput. Phys.* **48**, 387–411.

Haj-Hariri, H. & Homsy, G. M. 1997 Three-dimensional instability of viscoelastic elliptic vortices. *J. Fluid Mech.* **353**, 357–381.

Kelmanson, M. A. & Lonsdale, B. 1996 Eddy genesis in the double-lid-driven cavity. *Q. J. Mech. Appl. Maths* **49**, 635–655.

Kuhlmann, H. C., Wanschura, M. & Rath, H. J. 1997 Flow in two-sided lid-driven cavities: Non-uniqueness, instabilities, and cellular structures. *J. Fluid Mech.* **336**, 267–299.

Kuhlmann, H. C., Wanschura, M. & Rath, H. J. 1998 Elliptic instability in two-sided lid-driven cavity flow. *Eur. J. Mech.* B/*Fluids* **17**, 561–569.

Landman, M. J. & Saffman, P. G. 1987 The three-dimensional instability of strained vortices in a viscous fluid. *Phys. Fluids* **30**, 2339–2342.

Lifshitz, A. & Hameiri, E. 1991 Local stability conditions in fluid dynamics. *Phys. Fluids* A **3**, 2644–2651.

Lundgren, T. S. & Mansour, N. N. 1996 Transition to turbulence in an elliptic vortex. *J. Fluid Mech.* **307**, 43–62.

Manneville, P. & Dauchot, O. 2001 Patterning and transition to turbulence in subcritical systems:

https://doi.org/10.1017/S0022112002007917 Published online by Cambridge University Press

the case of plane Couette flow. In *Coherent Structures in Complex Systems* (ed. D. Reguera, L. L. Bonilla & J. M. Rubi), pp. 58–79. Springer.

Moffatt, H. K. 1964 Viscous and resistive eddies near a sharp corner. *J. Fluid Mech.* **18**, 1–18.

Moore, D. W. & Saffman, P. G. 1975 The instability of a straight vortex filament in a strain field. *Proc. R. Soc. Lond.* A **346**, 413–425.

Pan, F. & Acrivos, A. 1967 Steady flows in rectangular cavities. *J. Fluid Mech.* **28**, 643–655.

Pierrehumbert, R. T. 1986 Universal short-wave instability of two-dimensional eddies in an inviscid fluid. *Phys. Rev. Lett.* **57**, 2157–2159.

Ramanan, N. & Homsy, G. M. 1994 Linear stability of lid-driven cavity flow. *Phys. Fluids* **8**, 2690–2701.

Saffman, P. G. 1992 *Vortex Dynamics*. Cambridge University Press.

Shankar, P. N. & Deshpande, M. D. 2000 Fluid mechanics in the driven cavity. *Annu. Rev. Fluid Mech.* **32**, 93–136.

Sipp, D. & Jacquin, L. 1998 Elliptic instability in two-dimensional flattened Taylor–Green vortices. *Phys. Fluids* **10**, 839–849.

Sipp, D. & Jacquin, L. 2000 Three-dimensional centrifugal-type instabilities of two-dimensional flows in rotating systems. *Phys. Fluids* **12**, 1740–1748.

Sipp, D., Lauga, E. & Jacquin, L. 1999 Vortices in rotating systems: Centrifugal, elliptic and hyperbolic type instabilities. *Phys. Fluids* **11**, 3716–3728.

Taylor, G. I. 1934 The formation of emulsions in definable fields of flow. *Proc. R. Soc. Lond.* A **146**, 501–523.

Tillmark, N. & Alfredsson, P. H. 1992 Experiments on transition in plane Couette flow. *J. Fluid Mech.* **235**, 89–102.

Tsai, C.-Y. & Widnall, S. E. 1976 The stability of short waves on a straight vortex filament in a weak externally imposed strain field. *J. Fluid Mech.* **73**, 721–733.

Waleffe, F. 1990 On the three-dimensional instability of strained vortices. *Phys. Fluids* A **2**, 76–80.

Widnall, S. E. & Tsai, C.-Y. 1977 The instability of the thin vortex ring of constant vorticity. *Proc. R. Soc. Lond.* **287**, 273–305.

https://doi.org/10.1017/S0022112002007917 Published online by Cambridge University Press